SCIENTIFIC REPORTS

OPEN

Self-passivating (Re,Al)B_2 coatings synthesized by magnetron sputtering

Received: 3 September 2018
Accepted: 9 October 2018
Published online: 22 October 2018

Pascal Bliem, Stanislav Mráz, Sandipan Sen, Oliver Hunold & Jochen M. Schneider

($Re_{0.67}Al_{0.10}$)B_2 and ($Re_{0.74}Al_{0.11}$)B_2 solid solution as well as $Re_{0.85}B_2$ thin films were deposited by hybrid RF-DC magnetron sputtering. X-ray diffraction (XRD) showed that all films exhibit the ReB_2 (*P6₃/mmc*) crystal structure. X-ray photoelectron spectroscopy (XPS) analyses performed on atmosphere exposed thin film surfaces suggest that ReB_2 corrodes, consistent with literature, by forming perrhenic acid ($HReO_4$) already after two days, while ($Re_{0.74}Al_{0.11}$)B_2 forms a self-passivating Al-oxide layer preventing corrosion in a time period $\geq$ 60 days. Hence, it is evident that Al additions to ReB_2 significantly increase the chemical stability during atmosphere exposure.

The increasing number of highly specialized industrial machining applications creates a demand for suitable new hard coating material systems. Commonly known superhard ($H \geq 40$ GPa) materials such as diamond (up to 150 GPa), cubic BN (up to 80 GPa)[1], B_6O (up to 45 GPa)[2], and cubic BC_2N (up to 75 GPa)[3], are all electrical insulators and can sometimes not be utilized, e.g. during machining of ferrous alloys with diamond-like coatings[4] due to carbide formation. Borides are used as hard and wear-resistant coatings[5], e.g. in Al machining due to low Al adhesion on the coated tool surface[6]. ReB_2 (*P6₃/mmc*), first synthesized in 1962 by La Placa *et al.*[7], is metallic[8] and was first suggested to exhibit a hardness above 40 GPa little more than a decade ago by Chung *et al.*[4]. Density functional theory calculations of ReB_2[9–12] show that B-B and Re-B bonds are short and highly directionally covalent, therefore strong, whereas Re-Re bonds are predominantly metallic.

Chung *et al.*[4] reported a hardness of 48 GPa at 0.5 N indentation load which, however, decreased with increasing load down to 30 GPa at 5 N load. Other experimental studies report largely scattered values of measured hardness ($H = 38(11)$ GPa[4,13–18], notation: average value (standard deviation on the last significant digits)). One reason for this scattering can be the presence Re_7B_3 phase impurities which are often reported[17,19–22] and which highlight the necessity of obtaining phase-pure samples for a reliable characterization. Despite several of the studies mentioned above have suggested that ReB_2 may be a promising candidate for hard coating applications, only two studies have synthesized ReB_2 thin films by pulsed laser deposition[15,18]. Experiments employing methods which can be used on large industrial scales, such as magnetron sputtering, are yet lacking.

Besides the need for further research on thin film synthesis, there is a necessity to evaluate the material's chemical stability. Two studies[16,23] reported formation of a viscous liquid layer on their samples exposed to air. Orlovskaya *et al.*[23] hypothesized that on their mechanically milled powders, Re_2O_7 and B_2O_3 oxides react with water from air and form perrhenic acid ($HReO_4$) and boric acid (H_3BO_3), respectively. Due to hygroscopicity of these acids, they may adsorb further water from air and continue to degrade the bulk material. The authors' hypothesis was based on thermodynamic data and not proven experimentally. Very recently, Granados-Fitch *et al.*[24] extended Orlovskaya *et al.*'s work by experimentally studying the reaction of mechanically milled powders in humid air over duration of 26 months. Theses ReB_2 powders decomposed entirely into $HReO_4$ (liquid), H_3BO_3, HBO_2, and ReO_3. The corrosive reaction is possibly accelerated by the catalytic activity of perrhenic acid[25,26].

Alloying of Al may represent a method to counteract the potential corrosive reaction. The addition of Al to TiN thin films results in the formation of alumina upon oxidation and an improved oxidation resistance of the ternary TiAlN, compared to the binary TiN[27]. Even in borides with a small Al content, such as amorphous $AlYB_{14}$, Al is preferentially oxidized[5]. Furthermore, Al is not only known for its oxygen affinity and stable Al_2O_3 oxide which is commonly used as a diffusion barrier[28]; it also forms a hexagonal diboride AlB_2 (*P6/mmm*) (though not isostructural to ReB_2 as B layers in AlB_2 are flat and not puckered). It has been shown previously that alloying W, which also forms a hexagonal diboride WB_2 (*P6₃/mmc*) with both flat and puckered B layers, into ReB_2 can yield

Materials Chemistry, RWTH Aachen University, Kopernikusstr. 10, D-52074, Aachen, Germany. Correspondence and requests for materials should be addressed to P.B. (email: pascal.bliem@rwth-aachen.de)

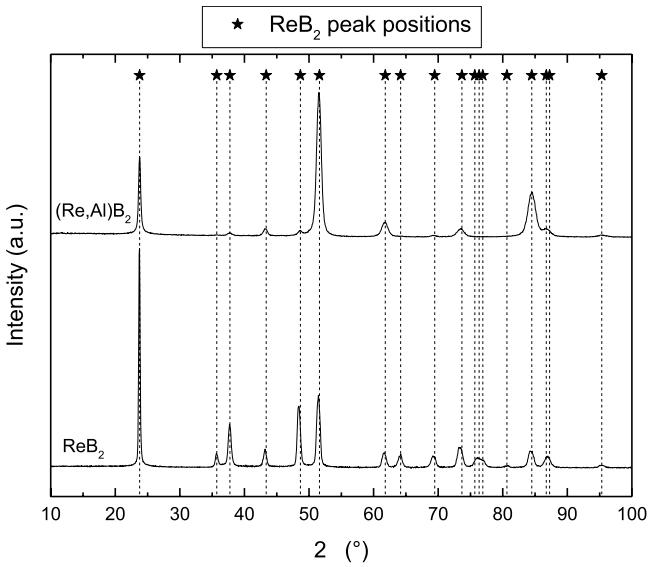

Figure 1. X-ray diffractogramms of studied samples. Shown are diffractograms of $Re_{0.85}B_2$ (bottom curve) and $(Re_{0.67}Al_{0.10})B_2$ (top curve) films. Peak positions of the ReB_2 crystal structure (JCPDS card 00-11-5081) are indicated by markers with drop-lines.

in solid solutions with high hardness (up to 48 GPa)[29]. Hence, it is promising to investigate Al solubility in ReB_2 with its inherently strong B-B and metal-B bonds and the mechanical properties of such solid solution thin films.

Herein, it will be demonstrated that $Re_{0.85}B_2$ as well as $(Re_{0.67}Al_{0.10})B_2$ and $(Re_{0.74}Al_{0.11})B_2$ thin films synthesized by RF-DC magnetron sputtering exhibit the ReB_2 ($P6_3/mmc$) structure. Additionally, an investigation of surface chemical reactions by X-ray photoelectron spectroscopy (XPS) will show that the $Re_{0.85}B_2$ thin film corroded upon exposure to atmosphere by forming perrhenic acid, whereas the $(Re_{0.74}Al_{0.11})B_2$ thin film formed a passivating Al-oxide layer suppressing a corrosive reaction. Furthermore, nanoindentation data will be compared to ab initio predictions of the elastic properties.

Results and Discussion

Diffractograms of both $Re_{0.85}B_2$ and $(Re_{0.67}Al_{0.10})B_2$ films (Fig. 1., bottom and top curves, respectively) utilized for further mechanical characterization only display peaks attributable to the ReB_2 crystal structure (JCPDS card 00-11-5081). No other Re-B phases or Al-borides are detected by XRD; hence, it is reasonable to assume that the 3.5 at.% Al in $(Re_{0.67}Al_{0.10})B_2$ is dissolved in the ReB_2 crystal lattice and a solid solution is formed. While the Al concentration induced changes in lattices parameters measured by XRD ($\Delta a = +0.31\%$, $\Delta c = -0.31\%$) are opposite in trend to the values predicted by DFT ($\Delta a = -0.08\%$, $\Delta c = +0.25\%$), it has to be noted that the magnitude of the obtained deviations are according to Paier *et al.*[30] in line with the exchange-correlation functionals employed here.

The films appear slightly B over-stoichiometric, potentially resulting in segregation of an amorphous B tissue phase[31] or Re sub-lattice vacancies[32]. This is not further investigated here. Considering the measurement technology (energy dispersive X-ray spectroscopy) inherent errors which, according to Goldstein *et al.*[33] can be larger than ±5% (relative) for rough samples and compounds containing light elements, the stoichiometric diboride composition lies within the error bars. For the chemical quantification, only intentionally introduced elements are considered here; however the samples contain C (ca. 4.5 at.%), O (ca. 1.0 at.%) and Fe (ca. 1.0 at.%) impurities, probably stemming from the B targets, residual gas contamination[34], and RF sputtered chamber walls, respectively.

Surface chemical reactivity of $Re_{0.85}B_2$ in air was analyzed employing XPS measurements. The sample investigated here was transferred to the XPS system immediately after deposition. The initial air exposure time was less than 120 seconds. Subsequent measurements are conducted after exposing the sample to atmosphere for 2 days and 13 days. High resolution XPS spectra of the B 1 s and Re 4 f transitions are shown in Fig. 2(a,b), respectively. The bottom panels show the scans recorded right after the deposition. The minor signals that can be observed at lower binding energies next to the main signals are satellite peaks introduced by the non-monochromatic Al K_α radiation. The main B 1 s signal stemming from ReB_2 is located at 187.9 eV. Information on the fitting of other components in the XPS spectra can be found in the supplementary material.

After two days in air, the lower peak-to-background ratio indicates a strongly decreased intensity of the B 1 s signal. A strong new component emerges at 46.5 eV in the Re 4 f scan, which can be assigned to the perrhenate ion (ReO_4^-)[26]. The ReO_4^- ion is a constituent of Re_2O_7, which, when solved in water, forms perrhenic acid[35]. After 13 days in air, the Re 4 f signal consists almost completely of the ReO_4^- component and the B 1 s signal has entirely disappeared. Over less than two weeks, the surface of $Re_{0.85}B_2$ becomes covered by several nanometers of perrhenic acid, taking into account that XPS depth resolution is in the order of a few nanometers and the B 1 s signal is undetectable. Orlovskaya *et al.*'s[23] hypothesis about and Granados-Fitch *et al.*'s[24] observation of formation

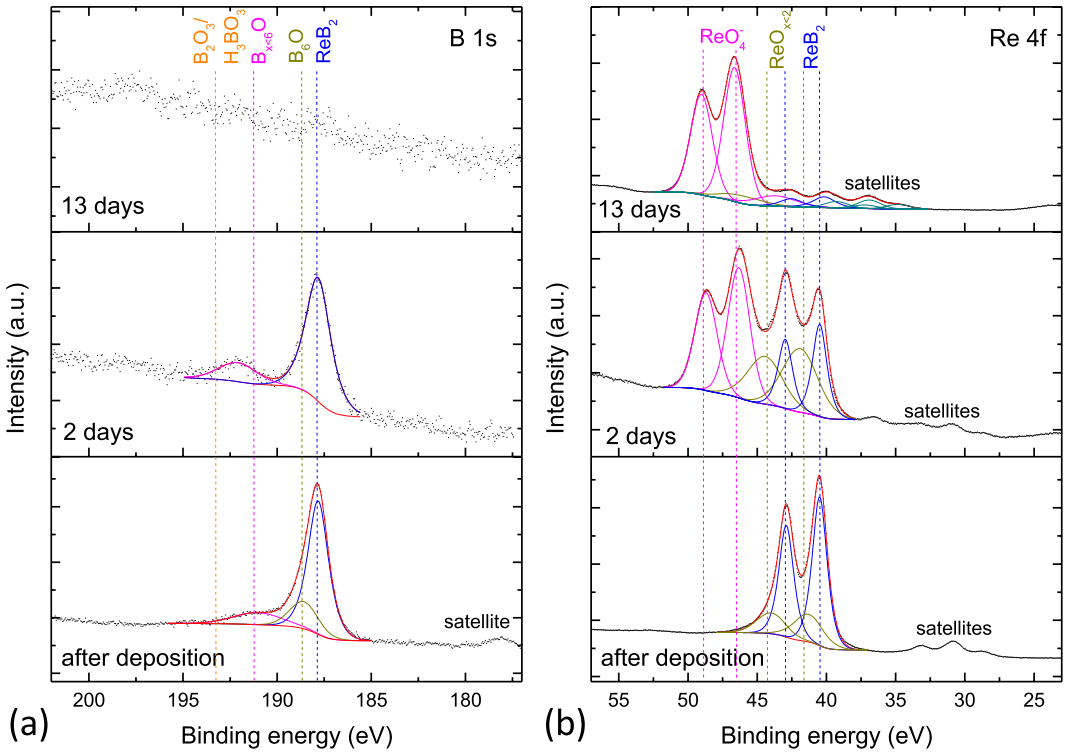

Figure 2. XPS scans of $Re_{0.85}B_2$. Shown are spectra of the (**a**) B 1 s and (**b**) Re 4 f transitions after different air exposure durations. The position of the components fitted to the spectra is indicated by drop-lines.

of perrhenic acid during atmosphere exposure mechanically milled powders are confirmed here for thin films. There is no evidence for the formation of boric acid or ReO_3 in this corrosion stage.

High resolution XPS spectra of the B 1 s, Re 4 f, and Al 2 s transitions of an $(Re_{0.74}Al_{0.11})B_2$ film after different air exposure durations are shown in Fig. 3(a–c), respectively. The Al 2 s transition is used instead of the more commonly used 2p transition because the latter is convoluted with the Re 4 f energy loss background. After approximately six hours in air, there is only one Al-oxide component in the Al 2 s signal located at 119.0 eV, which coincides excellently with literature values of Al_2O_3[36]. It should be noted that this means that the bonding environment and the resulting electron binding energy is comparable to that of Al_2O_3; it does not necessarily mean that the composition of the Al-oxide measured here is exactly that of Al_2O_3 and one cannot infer in which phase it is present. In the B 1 s scan, only the component of $(Re,Al)B_2$ at 187.4 eV can be observed. The Re 4 f signal, similar to the unalloyed sample, shows the main $(Re_{0.74}Al_{0.11})B_2$ component located at 40.2 eV and a smaller component at 41.0 eV, which may originate from incipient oxidation or impurity bonds as discussed previously. After three days in air (measured but not shown in Fig. 3.), Al and B signals do not exhibit any change. A minor component located at higher binding energy (46.0 eV, labeled as $ReO_{3<x<4}$ here), which exhibits an oxidation state between ReO_3 and ReO_4^-, emerges in the Re 4 f scan. After 16 days in air (center panels in Fig. 3), this component increases only minimally from 4.2 to 5.1% of the total integrated intensity. Al and B spectra do still not show any change. After 66 days in air, small oxidized components ($B_{x<6}O$, B_6O) appear in the B 1 s spectrum; however, these components together make up only 13.7% of the total integrated intensity of the B signal, showing that B is not significantly oxidized after 66 days. The oxidized component in the Re 4 f spectrum, *i*, is increased to only 5.6% of the total integrated intensity after 66 days atmosphere exposure, so exhibiting approximately a $3.83 \times t^{0.09}$ dependence, where *t* is the oxidation time in days. From a practical perspective, passivation of the film is achieved since *i* increases by only 0.05% from 4.71% after 9 days to 4.76% after 10 days of the film air exposure. Furthermore, no N is detected in this film. Initially, Re oxidizes a little while the Al-oxide layer is not fully evolved; nonetheless, the Al-oxide seems to passivate the film in the long term. Even if this passivation is mechanically destroyed (e.g. by wear), the Al-oxide layer will be restored since Al is incorporated in the ReB_2 structure.

Hardness and elastic modulus measured by nanoindentation are given in Table 1. The $Re_{0.85}B_2$ film ($H_{exp} = 32$ GPa, $E_{exp} = 522$ GPa) does, on average, exhibit a hardness which is lower than the average of previously reported values ($H_{lit} = 38(11)$ GPa[4,13–18]) and the elastic modulus is 21.7% lower than theoretically predicted ($E_{DFT} = 667$ GPa). The standard deviation on both quantities is with 25.7% relatively large. The $(Re_{0.67}Al_{0.10})B_2$ film, on the contrary, shows a higher hardness of 40 GPa, higher stiffness ($E = 562$ GPa, 7.7% higher than $Re_{0.85}B_2$), and lower standard deviations on the measured quantities. For both films, the indentation depth does not exceed the conventional 10% of the film thickness (Table 1); hence, a substrate influence is unlikely to explain the significant difference in measured mechanical properties. Instead, the measured surface roughness (Table 1) indicates that the $Re_{0.85}B_2$ film is much rougher than the $(Re_{0.67}Al_{0.10})B_2$ film. The $Re_{0.85}B_2$ film's measured root mean square surface roughness of 38(1) nm is considerably large compared to the indenter tip radius of 100 nm. When

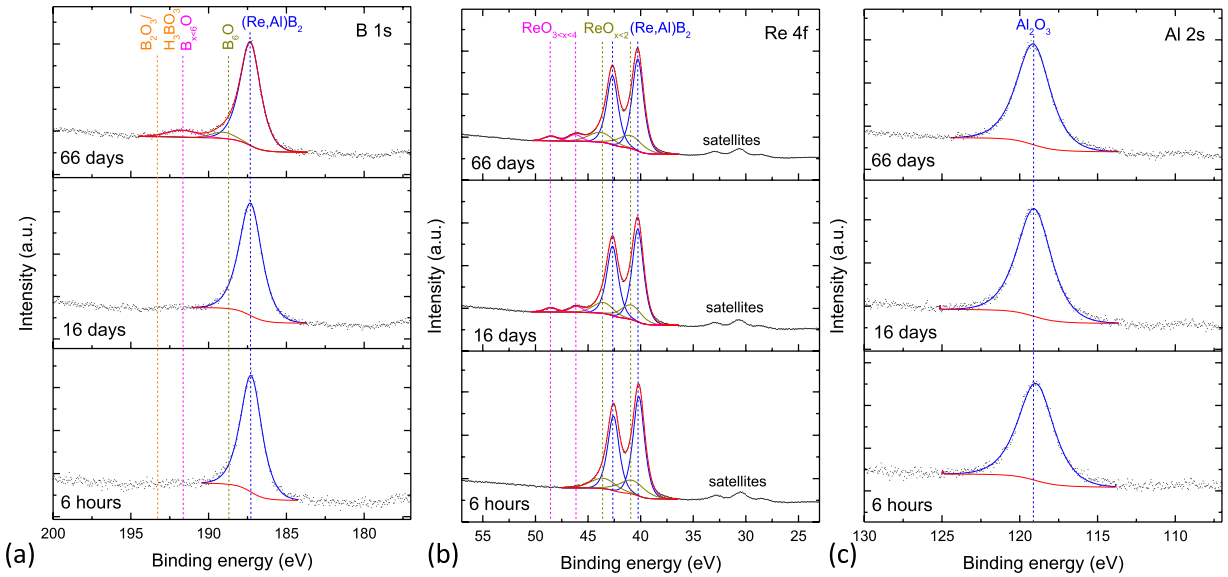

Figure 3. XPS scans of $(Re_{0.74}Al_{0.11})B_2$. Shown are spectra of the (**a**) B 1 s, (**b**) Re 4 f, and (**c**) Al 2 s transitions after different air exposure durations. The position of the components fitted to the spectra is indicated by droplines.

Sample	at.% B	at.% Al	*H* (GPa)	*E* (GPa)	E_{DFT}(GPa)	*h* (nm)	*D* (μm)	R_q (nm)
$Re_{0.85}B_2$	70.1	0.0	32(9)	522(134)	667	90(17)	1.52(6)	38(1)
$(Re_{0.67}Al_{0.10})B_2$	72.4	3.5	40(5)	562(56)	621	72(8)	1.83(9)	18(2)[a]

Table 1. Chemical composition and nanoindentation data for $Re_{0.85}B_2$ and $(Re_{0.67}Al_{0.10})B_2$ films. The columns display B and Al concentrations, average values of measured (standard deviation on the last significant digit is given in parenthesis) hardness, *H*, elastic modulus, *E*, indentation depth, *h*, film thickness, *D*, and root mean square surface roughness, R_q. [a]Resolution of the microscope is given as 20 nm. The stated value might overestimate the actual R_q.

indenting into a surface asperity, there is no continuous material on the sides opposing plastic deformation. The $(Re_{0.67}Al_{0.10})B_2$ film's surface roughness of 18(2) nm lies below the microscope's assumed resolution limit of 20 nm, suggesting 18 nm to be an upper limit of the surface roughness. The 100 nm radius indenter, therefore, indents into a continuous film rather than into surface asperities. This may contribute to the lower measured average and higher scattering of *H* and *E* of the rougher ReB_2 film. The presence of porosity in the films may affect these quantities as well. A stark difference in surface roughness between the two films and indications for porosity in the $Re_{0.85}B_2$ film can be seen in SEM images in the supplementary information in Figs S1 and S2.

In summary, $(Re_{0.67}Al_{0.10})B_2$ and $(Re_{0.74}Al_{0.11})B_2$ solid solution and $Re_{0.85}B_2$ films were synthesized by hybrid RF-DC magnetron sputtering. All films crystalize in the ReB_2 ($P6_3/mmc$) crystal structure, as probed by XRD. $Re_{0.85}B_2$ reacts in humid air and forms perrhenic acid already after two days of atmosphere exposure, as shown by XPS. This corrosive reaction renders unalloyed ReB_2 coatings unsuitable for application in humid air. Upon atmosphere exposure at room temperature $(Re_{0.74}Al_{0.11})B_2$, however, forms a self-passivating Al-oxide layer retarding the formation of perrhenic acid and, hence, corrosion. It is evident that Al additions to ReB_2 significantly increase the chemical stability during atmosphere exposure.

Methods

Experimental details. $(Re_{0.67}Al_{0.10})B_2$, $(Re_{0.74}Al_{0.11})B_2$ and $Re_{0.85}B_2$ films were deposited by magnetron sputtering at 900 °C in a vacuum chamber accommodating four magnetrons (50 mm diameter) tilted to the substrate normal by 20° at a substrate-target distance of 12.4 cm. The average base pressure laid below 6.67×10^{-5} Pa (5×10^{-7} Torr). Ar was used as sputtering gas at constant working pressure of 0.67 Pa (5×10^{-3} Torr). The substrates' backsides were coated with Mo for a better intake of radiative heat from the heater and, prior to deposition, the substrates were baked out for 20 minutes at deposition temperature. Re and Al targets were sputtered with direct current (DC) power supplies, while two B targets, facing each other, were sputtered by radio frequency (RF) power supplies.

Two $Re_{0.85}B_2$ samples were synthesized under identical conditions in the same batch (20 W at Re target, 2×148 W at B targets, 150 minutes) on polished MgO substrates at symmetry-equivalent positions on a rotating sample holder. The $(Re_{0.67}Al_{0.10})B_2$ sample was taken from a selected area of a combinatorial deposition (no rotation, 20 W at Re target, 7 W at Al target, 2×149 W at B targets, 150 minutes) on polished MgO. The $(Re_{0.74}Al_{0.11})$

B_2 sample was taken from a selected area of another combinatorial deposition (no rotation, 15 W at Re target, 5 W at Al target, 2 × 150 W at B targets, 60 minutes) on polished sapphire.

The phase composition was analyzed by X-ray diffraction (XRD) employing Cu K_α radiation (U = 40 kV, I = 40 mA) at a constant incident angle $\omega = 10°$ and a 2θ range from 10° to 100° in a Bruker AXS D8 Discover General Area Detection Diffraction System (GADDS). Cross-sectional scanning electron microscope (SEM) images, taken in a FEI Helios 660 system, were employed for film thickness determination. Root mean square surface roughness was measured by confocal laser scanning microscopy in a Keyence VK-9700 system (resolution limit ca. 20 nm) on 1000 μm^2 areas. Hardness and elastic modulus were investigated by nanoindentation with a 100 nm radius Berkovich diamond tip at 10 mN load in a depth-sensing nanoindenter (Hysitron TriboIndenterTM). 100 indentations were performed for each sample for sufficient statistics. A fused silica standard measured before and after the deposited films was used to calibrate the tip area function. Load-displacement curves exhibiting pop-in events (only one) were not considered for analysis. The Oliver-Pharr method[37] was applied to obtain the reduced elastic modulus. A Poisson's ratio of 0.18[38] was assumed for the samples to calculate the samples' elastic moduli.

The chemical composition of the films was quantified by energy dispersive X-ray spectroscopy (EDX) with an EDAX Genesis 2000 analyzer in a JEOL JSM-6480 SEM at an electron beam acceleration voltage of 5 kV. Chemical composition of the synthesized films was measured directly after the deposition and samples were stored in a high vacuum vessel (5.5×10^{-5} Pa base pressure) between all measurements due to the expected reactivity. One $Re_{0.85}B_2$ sample and the $(Re_{0.74}Al_{0.11})B_2$ sample were stored in air to evaluate their chemical stability. Chemical states at the surface of these two samples were investigated by XPS in a JEOL JAMP-9500F system with an Al K_α x-ray source (1486.5 eV), a hemispherical electron energy analyzer in fixed analyzer transmission mode with a pass energy of 20 eV, and an electron take-off angle perpendicular to the analyzer. The energy resolution is approximately 0.15 eV. For energy calibration, the Cu 2p 3/2 and 3p 3/2 lines (Ar^+ cleaned) were employed. Charging of the sample was corrected against the C 1 s peak (284.8 eV) of adventitious carbon. Voigt functions and Shirley backgrounds were used for fitting the data.

Computational details. Electronic structure calculations were used to calculate elastic properties of the pure ReB_2 system and systems in which Re is randomly substituted by varying concentrations of Al. The systems considered contained 0.0, 3.1, and 8.6 at% of Al. Values of calculated lattice parameters and elastic moduli for the experimentally found compositions have been linearly interpolated. All supercells contained 162 atoms. The calculations were performed within the framework of density functional theory (DFT) employing the Vienna Ab initio Simulation Package (VASP)[39]. Projector-augmented wave potentials within PBE-GGA[40] were used, for which the projector functions were evaluated in real space. Tetrahedron method smearing with Blöchl corrections[41] was used with an electronic convergence criterion of 10^{-4} eV. All systems were structurally relaxed applying a conjugate-gradient algorithm with a force convergence criterion of 10^{-2} eV/Å. The equilibrium volume was found by a Birch-Murnaghan equation of state[42,43] fit and the c/a-ratio was optimized by a third order polynomial fit. Cutoff energies of basis sets were equal to the distributor's recommended value for the respective potential during dynamic relaxation and were further increased by 25% for static calculations. Integration in the Brillouin zone was performed on Γ-point-centered Monkhorst-Pack[44] k-point grids converged to ≤1 meV per atom. Elastic constants were calculated by applying deformations to the cell geometry and fitting the change in total energy quadratically. Details were presented by Fast *et al.*[45]. Macroscopic elastic quantities (elastic modulus and Poission's ratio) were calculated from elastic constants using the Hill (Reuss-Voigt-average) method[46].

All data generated or analyzed during this study are included in this published article and its supplementary information files.

References

1. McMillan, P. F. New materials from high-pressure experiments. *Nat. Mater.* **1**, 19 (2002).
2. He, D. *et al.* Boron suboxide: As hard as cubic boron nitride. *Appl Phys Lett.* **81**, 643–645 (2002).
3. Solozhenko, V. L., Andrault, D., Fiquet, G., Mezouar, M. & Rubie, D. C. Synthesis of superhard cubic BC_2N. *Appl Phys Lett.* **78**, 1385–1387 (2001).
4. Chung, H.-Y. *et al.* Synthesis of Ultra-Incompressible Superhard Rhenium Diboride at Ambient Pressure. *Science* **316**, 436–439 (2007).
5. Hunold, O. *et al.* Influence of O_2 exposure on the interaction between CH_4 and amorphous $AlYB_{14}$. *Appl. Surf. Sci.* **392**, 1165–1172 (2017).
6. Berger, M. & Hogmark, S. Evaluation of TiB_2 coatings in sliding contact against aluminium. *Surf. Coat. Tech.* **149**, 14–20 (2002).
7. La Placa, S. J. & Post, B. The crystal structure of rhenium diboride. *Acta Cryst.* **15**, 97–99 (1962).
8. Żogał, O. J. *et al.* Crystal structure, electric field gradient, and electronic charge densities in ReB_2: A single crystal x-ray, B^{11} nuclear magnetic resonance, and first-principles study. *J. Appl. Phys.* **106**, 033514 (2009).
9. Zhu, X., Li, D. & Cheng, X. Elasticity properties of the low-compressible material ReB_2. *Solid State Commun.* **147**, 301–304 (2008).
10. Peng, F., Liu, Q., Fu, H. & Yang, X. Electronic and thermodynamic properties of ReB_2 under high pressure and temperature. *Solid State Commun.* **149**, 56–59 (2009).
11. Aydin, S. & Simsek, M. First-principles calculations of MnB_2, TcB_2, and ReB_2 within the ReB_2-type structure. *Phys. Rev. B* **80**, 134107 (2009).
12. Liang, Y., Li, A., Zhao, J. & Zhang, W. Designing superhard materials by incorporating boron into heavy transition metals. *Mod. Phys. Lett. B* **23**, 1281–1290 (2009).
13. Qin, J. *et al.* Is Rhenium Diboride a Superhard Material? *Adv. Mater.* **20**, 4780–4783 (2008).
14. Levine, J. B. *et al.* Preparation and Properties of Metallic, Superhard Rhenium Diboride Crystals. *J. Am. Chem. Soc.* **130**, 16953–16958 (2008).
15. Latini, A. *et al.* Superhard Rhenium Diboride Films: Preparation and Characterization. *Chem. Mater.* **20**, 4507–4511 (2008).
16. Otani, S., Korsukova, M. M. & Aizawa, T. High-temperature hardness of ReB_2 single crystals. *J. Alloy Compd.* **477**, L28–L29 (2009).
17. Levine, J. B. *et al.* Full elastic tensor of a crystal of the superhard compound ReB2. *Acta Mater.* **58**, 1530–1535 (2010).
18. Chrzanowska, J., Hoffman, J., Denis, P., Giżyński, M. & Mościcki, T. The effect of process parameters on rhenium diboride films deposited by PLD. *Surf. Coat. Tech.* **277**, 15–22 (2015).

19. Meschel, S. V. & Kleppa, O. J. Standard enthalpies of formation of NbB_2, MoB, and ReB_2 by high-temperature direct synthesis calorimetry. *Metall. Mater. Trans. A* **24**, 947–950 (1993).
20. Locci, A. M., Licheri, R., Orrù, R. & Cao, G. Reactive Spark Plasma Sintering of rhenium diboride. *Ceram. Int.* **35**, 397–400 (2009).
21. Tkachev, S. N. *et al*. Shear Modulus of Polycrystalline Rhenium Diboride Determined from Surface Brillouin Spectroscopy. *Adv. Mater.* **21**, 4284–4286 (2009).
22. Liu, X. *et al*. Isotropic Thermal Expansivity and Anisotropic Compressibility of ReB_2. *Chinese Phys. Lett.* **28**, 036401 (2011).
23. Orlovskaya, N. *et al*. Mechanochemical synthesis of ReB_2 powder. *J. Mat. Res.* **26**, 2772–2779 (2011).
24. Granados-Fitch, M. G., Quintana-Melgoza, J. M., Juarez-Arellano, E. A. & Avalos-Borja, M. Chemical stability of superhard rhenium diboride at oxygen and moisture ambient environmental conditions prepared by mechanical milling. *J. Am. Ceram. Soc.* n/a–n/a https://doi.org/10.1111/jace.15461.
25. Nikonova, O. A. *et al*. Novel approach to rhenium oxide catalysts for selective oxidation of methanol to DMM. *J. Catal.* **279**, 310–318 (2011).
26. Naor, A., Eliaz, N., Burstein, L. & Gileadi, E. Metals on Electrodeposition of Rhenium. *Electrochem. Solid St.* **13**, D91–D93 (2010). Direct Experimental Support for the Catalytic Effect of Iron-Group.
27. Münz, W. D. Titanium aluminum nitride films: A new alternative to TiN coatings. *J. Vac. Sci. Technol. A* **4**, 2717–2725 (1986).
28. Müller, J., Schierling, M., Zimmermann, E. & Neuschütz, D. Chemical vapor deposition of smooth α-Al_2O_3 films on nickel base superalloys as diffusion barriers. *Surf. Coat. Tech.* **120–121**, 16–21 (1999).
29. Lech, A. T. *et al*. Superhard Rhenium/Tungsten Diboride Solid Solutions. *J. Am. Chem. Soc.* **138**, 14398–14408 (2016).
30. Paier, J. *et al*. Screened hybrid density functionals applied to solids. *J. Chem. Phys.* **124**, 154709 (2006).
31. Mockute, A. *et al*. Age hardening in $(Ti_{1-x}Al_x)B_{2+\Delta}$ thin films. *Scripta Mater.* **127**, 122–126 (2017).
32. Portnoi, K. I. & Romashov, V. M. Phase diagram of the system rhenium-boron. *Sov. Powder Metall. Met. Cer.* **7**, 112–114 (1968).
33. Goldstein, J. I. *et al*. *Scanning Electron Microscopy and X-ray Microanalysis*. (Springer, US, Boston, MA: 2003).
34. Schneider, J. M., Hjörvarsson, B., Wang, X. & Hultman, L. On the effect of hydrogen incorporation in strontium titanate layers grown by high vacuum magnetron sputtering. *Appl. Phys. Lett.* **75**, 3476–3478 (1999).
35. Beyer, H., Glemser, O. & Krebs, B. Dirhenium Dihydratoheptoxide $Re_2O_7(OH_2)_2$ – New Type of Water Bonding in an Aquoxide. *Angew. Chem. Int. Ed. Engl.* **7**, 295–296 (1968).
36. National Institute of Standards and Technology, NIST X-ray Photoelectron Spectroscopy Database, Version 4.1., Gaithersburg MD, 20899 (2000)
37. Oliver, W. C. & Pharr, G. M. An improved technique for determining hardness and elastic modulus using load and displacement sensing indentation experiments. *J. Mat. Res.* **7**, 1564–1583 (1992).
38. Liang, Y. & Zhang, B. Mechanical and electronic properties of superhard ReB_2. *Phys. Rev. B* **76**, 132101 (2007).
39. Kresse, G. & Furthmüller, J. Efficient iterative schemes for ab initio total-energy calculations using a plane-wave basis set. *Phys. Rev. B* **54**, 11169–11186 (1996).
40. Perdew, J. P., Burke, K. & Ernzerhof, M. Generalized Gradient Approximation Made Simple. *Phys. Rev. Lett.* **77**, 3865–3868 (1996).
41. Blöchl, P. E., Jepsen, O. & Andersen, O. K. Improved tetrahedron method for Brillouin-zone integrations. *Phys. Rev. B* **49**, 16223–16233 (1994).
42. Birch, F. Finite Elastic Strain of CubicCrystals. *Phys. Rev.* **71**, 809–824 (1947).
43. Murnaghan, F. The compressibility of media under extreme pressures. *Proc. Natl. Acad. Sci. USA* **30**, 244–247 (1944).
44. Monkhorst, H. J. & Pack, J. D. Special points for Brillouin-zone integrations. *Phys. Rev. B* **13**, 5188–5192 (1976).
45. Fast, L., Wills, J. M., Johansson, B. & Eriksson, O. Elastic constants of hexagonal transition metals: Theory. *Phys. Rev. B* **51**, 17431–17438 (1995).
46. Hill, R. Elastic properties of reinforced solids: Some theoretical principles. *J. Mech. Phys. Solids.* **11**, 357–372 (1963).

Acknowledgements

Computational resources provided by the Jülich-Aachen Research Alliance (JARA) (grant jara0151) are acknowledged. J.M.S. gratefully acknowledges financial support from the MPG fellow program. P.B. wants to express his gratitude to A.-N. Wang for fruitful discussions and support during the course of this work.

Author Contributions

P.B. conceived, designed and performed the research and wrote the paper. S.M. and S.S. helped in the design of the research, performed some experimental aspects of the research and co-wrote the paper. O.H. and J.M.S. helped in the design of the research and co-wrote the paper.

Additional Information

Supplementary information accompanies this paper at https://doi.org/10.1038/s41598-018-34042-1.

Competing Interests: The authors declare no competing interests.

Publisher's note: Springer Nature remains neutral with regard to jurisdictional claims in published maps and institutional affiliations.